Nanoscale
Advances

ROYAL SOCIETY
OF CHEMISTRY

PAPER

View Article Online
View Journal | View Issue

Check for updates

Cite this: *Nanoscale Adv.*, 2025, 7, 4908

Experimental and molecular dynamics study of laser-induced carbon nanosphere formation using nanosecond-pulsed lasers†

Cheol Hwan Kim, ‡[a] Chae Yoon Shin, ‡[a] Jun Uk Lee,‡[b] Sung-Yeob Jeong *[c] and Bo Sung Shin *[d]

Received 15th April 2025
Accepted 24th June 2025

DOI: 10.1039/d5na00358j

rsc.li/nanoscale-advances

In this study, carbon nanospheres (CNSs) were synthesized using a 450 nm wavelength nanosecond-pulsed laser, and their formation mechanism was theoretically elucidated through molecular dynamics simulations. It was observed empirically that the size of the formed particles varied with the fluence. The formation mechanism was verified using molecular dynamics simulations. The simulation results showed that the sp^3 hybridisation ratio was the highest within a specific temperature range, which was consistent with the three-dimensional carbon nanosphere formation observed in the experiments. In particular, the highest sp^3/sp^2 ratio was noted at 4200 K, demonstrating that this temperature range is optimal for the stable growth of three-dimensional CNSs. However, at higher temperatures, the number of sp^3 and sp^2 structures decreased, indicating that excessive temperatures hindered nanosphere formation. These results suggest that the size and structure of the CNSs can be controlled by adjusting the laser fluence, providing a fundamental basis for future applications of functional carbon-based nanospheres.

Introduction

Carbon-based materials are utilized in various fields owing to their abundance and excellent mechanical and chemical stability.[1–3] Among them, carbon nanospheres (CNSs) have received considerable attention owing to their unique spherical structure and potential applications in energy storage, gas adsorption,[4] drug transport,[5] and catalysis.[6] Several methods have been developed for synthesizing CNSs, including the template method,[7–11] hydrothermal carbonization,[12,13] Stöber method,[14–16] aerosol-assisted synthesis,[17] spray drying,[18,19] and chemical vapor deposition,[20] as introduced in Table 1. However, these techniques exhibit the following limitations:[21–24]

(i) Poor control over the size and morphology of CNSs often causes inconsistencies in surface area and pore structure, directly affecting material performance in applications, such as energy storage and catalysis.[24]

(ii) The use of corrosive or hazardous chemicals, which pose environmental and safety concerns and may introduce impurities or require further purification.[23,24]

(iii) The need for additional carbonization or post-processing steps, which increases energy input, extends processing time, and reduces the reproducibility of the synthesis.[22,24]

Recently, laser synthesis of carbon nanostructures has been widely studied. Although laser techniques have been studied for the synthesis of various carbon materials, such as carbon nanoparticles and graphene-like structures,[25–27] the controlled synthesis of CNSs with defined morphology and hybridisation states remains largely unexplored. A previous study reported the formation of CNSs *via* the laser irradiation of a gas precursor.[28] This method induces a photothermal effect by laser pulses, generating a spatially localised high-temperature region. However, this method requires high vacuum conditions and complex optical setups, which limit its direct fabrication.

In parallel, investigations on laser-induced graphene (LIG) formation from polyimide (PI) have demonstrated that different carbon-based nanostructures are formed depending on the laser fluence.[29] These findings suggest the possibility of tuning the carbon nanostructure formation by simple laser control under ambient condition. However, their chemical composition and formation mechanisms remain unclear. In this study, we aim to characterise the composition and structure of laser-induced spherical carbon nanostructures formed from PI films.

---

[a] *Department of Cogno-Mechatronics Engineering, Pusan National University, Busan, 46241, Republic of Korea*

[b] *Multifunctional Composites Manufacturing Laboratory (MCML), Department of Mechanical and Industrial Engineering, University of Toronto, Toronto, M5S 3G8, Canada*

[c] *Department of Mechanical Engineering, University of Tokyo, Tokyo, 113-8656, Japan. E-mail: ysjsykj8025@naver.com*

[d] *Department of Optics and Mechatronics Engineering, Pusan National University, Busan, 46241, Republic of Korea. E-mail: bosung@pusan.ac.kr*

† Electronic supplementary information (ESI) available. See DOI: **https://doi.org/10.1039/d5na00358j**

‡ Cheol Hwan Kim, Chae Yoon Shin, and Jun Uk Lee contributed equally to this work.

Table 1 Methods comparison for CNS synthesis

Method	Description	Precursor phase	Atmosphere	Patterning	Post-processing	References
Template method	Synthesizing CNS by coating carbon precursor on a template by carbonization	Solid	Ambient/inert gas	No	Yes	7–11
Hydrothermal carbonization	Treating biomass or sugars at 180–250 °C to obtain carbon spheres	Liquid	Sealed autoclave	No	Yes	12 and 13
Stöber method	Coating carbon precursor on silica spheres and removing template to form hollow CNS	Solid	Ambient/inert gas	No	Yes	14–16
Aerosol-assisted synthesis	Spraying carbon precursor aerosols into high-temperature flow for instantaneous decomposition	Aerosol	Inert gas	No	Yes	17
Spray drying	Solidifying precursor *via* high-temperature spraying and subsequent carbonization	Liquid	Ambient/inert gas	No	Yes	18 and 19
Chemical vapor deposition	Decomposing gaseous carbon precursors on heated metal catalysts at high temperature	Gas	Vacuum/inert gas	Limited	Yes	20
Laser synthesis	Laser-induced decomposition of gaseous precursors like CH_4 in vacuum to form CNS	Gas	Vacuum chamber	No	No	28
This work (PI + ns-laser)	Direct laser irradiation of solid PI film under ambient conditions to form CNS-like structures	Solid	Ambient	Yes	No	This study

To complement our experimental analysis, molecular dynamics (MD) simulation were performed using the Large-scale Atomic/Molecular Massively Parallel Simulator (LAMMPS) to investigate atomic interactions and structural changes under varying temperatures.[30,31] Specifically, reactive force field (ReaxFF) enables the accurate modelling of chemical bond formation and dissociation as well as π- and σ-bond interactions,[32–34] allowing for precise simulation of sp^2 to sp^3 hybridisation transitions in carbon structures.[35–37] By applying this method, we revealed the atomic-level mechanisms governing the formation of CNS-like carbon nanostructures from polyimide films under nanosecond pulsed laser irradiation.

We experimentally analysed the characteristics of nanostructures formed by laser processing under varying fluence conditions using field-emission scanning electron microscopy (FE-SEM) and Raman spectroscopy. In addition, we performed MD simulations to observe the temperature-induced structural evolution and hybridisation changes in the PI precursors at the atomic level. By combining experimental and theoretical analyses, this study investigates whether nanostructures formed on PI *via* laser processing exhibit characteristics analogous to conventional CNSs and explores the feasibility of an environmentally friendly, single-step synthesis route for CNS-like structures.

In particular, this study aimed to evaluate whether laser-induced nanostructures on PI films exhibit structural and chemical characteristics analogous to those of conventional CNSs. By combining experimental observations with MD-based theoretical modelling, we proposed a new route for the scalable and patternable synthesis of CNS-like carbon nanostructures under simplified and eco-friendly conditions.

Materials and methods

Laser processing

To observe the fluence-dependent geometry of the CNSs as a function of the focal length during laser processing, a 0.14 mm-thick PI film (Kapton, Dupont, USA) was tilted at 45°. Glass slides (Paul Marienfeld GmbH & Co. KG, Germany) measuring 76 mm × 26 mm and 1 mm thick, was placed on top of the PI film and irradiated with a laser to pattern the LIG.

A laser engraver (LaserPecker 2, LaserPecker, China) was used, with a laser power of 5 W, a wavelength of 450 nm, and a spot size of 50 μm at the focal length. The experimental setup is illustrated in Fig. 1. The laser fluence, which is the energy in joules delivered to the PI surface divided by its area, was calculated using eqn (1). The fluence varied with spot diameter based on the reciprocal of the squares.

$$\text{Fluence}\ \left[\mathrm{J\ cm^{-2}}\right] = \frac{W}{p \times \pi (d/2)^2} \tag{1}$$

where W is the laser power, d is the spot diameter, and p is the pulse-repetition frequency.

The fabricated samples were visually inspected for shape variations with changes in focal length. Further structural observations were performed using FE-SEM (GEMINI 500, Carl Zeiss, Germany) to analyse regions exhibiting unusual morphologies. Fig. 1 shows a schematic diagram of the overall experiment.

Size distribution analysis

To analyse the size distribution of the nanoscale spherical particles observed in the FE-SEM images, ImageJ software (ver. 1.54g) was used to quantify the number and size of the particles. To restrict analysis to only particles with near-spherical shapes,

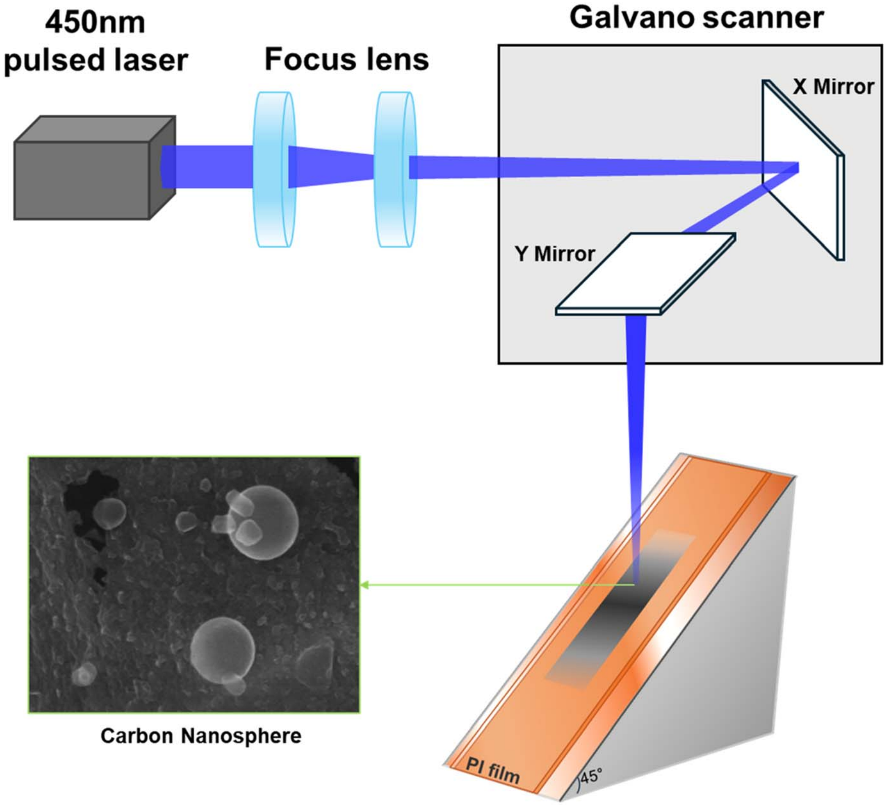

Fig. 1 Schematic diagram of 450 nm laser irradiation on the inclined PI film for subsequent position-dependent analysis.

only those with a circularity range of 0.70–1.00 were measured.[38] In addition, because of the heterogeneous morphology of the particles, which included both circular and elliptical shapes, the equivalent circular diameter (ECD) of each particle was calculated to analyse its diameter. The ECD was derived from the area values obtained using ImageJ software, based on the following equation:

$$\mathrm{ECD} = 2 \times \sqrt{\frac{\mathrm{Area}}{\pi}} \tag{2}$$

Size distribution histograms were constructed based on the measured ECDs and particle counts. Kernel density estimation (KDE) was performed using a Gaussian kernel to visualise the probability density function of the particle size distribution. KDE was calculated as follows:

$$\hat{f}(x) = \frac{1}{nh}\sum_{i=1}^{n} K\left(\frac{x - x_i}{h}\right) \tag{3}$$

where $\hat{f}(x)$ is the estimated density at point x; n is the number of data points; x_i is the observed data; h is the bandwidth; and K is the Gaussian kernel function.

The bandwidth h was determined using Scott's rule:[39]

$$h = \sigma \times n^{-1/5} \tag{4}$$

where σ is the standard deviation of the sample, and n is the number of data points.

To facilitate the comparison, the KDE curves were scaled to match the frequency range of the histograms. All the statistical analyses were performed using the Seaborn library in Python (ver. 3.9).

ReaxFF MD simulation

For molecular modelling, the Kapton monomer was placed at a density of 1.1 g cm^{-3} in 30.9 × 30.9 × 30.9 Å^3 cells, as shown in Fig. 2. MD analysis was performed using the LAMMPS software. ReaxFF was used to accurately calculate the π-bonds, σ-bonds, and interactions between atoms. The governing equations for the ReaxFF are as follows:

$$E_{\mathrm{system}} = E_{\mathrm{bond}} + E_{\mathrm{lp}} + E_{\mathrm{val}} + E_{\mathrm{over}} + E_{\mathrm{under}} + E_{\mathrm{Coulomb}} + E_{\mathrm{vdWaals}} \tag{5}$$

where E_{system} is the potential energy of the system, E_{bond} refers to the bond energies, E_{lp} denotes the lone pair energies, E_{val} corresponds to the energies related to the valence angles, E_{over} and E_{under} represent the energies necessary to correct the overcoordination and undercoordination of atoms, respectively, E_{Coulomb} denotes the non-bonded Coulomb energy, and E_{vdWaals} pertains to van der Waals interactions.

The simulation was run with a timestep of 0.05 fs and ramped from 50 K to 300 K at 10 ps intervals under initial *NVT* conditions, and then held for 10 ps to stabilise. It was ramped to the target temperature (3800, 4200, 4600, or 5000 K) and held

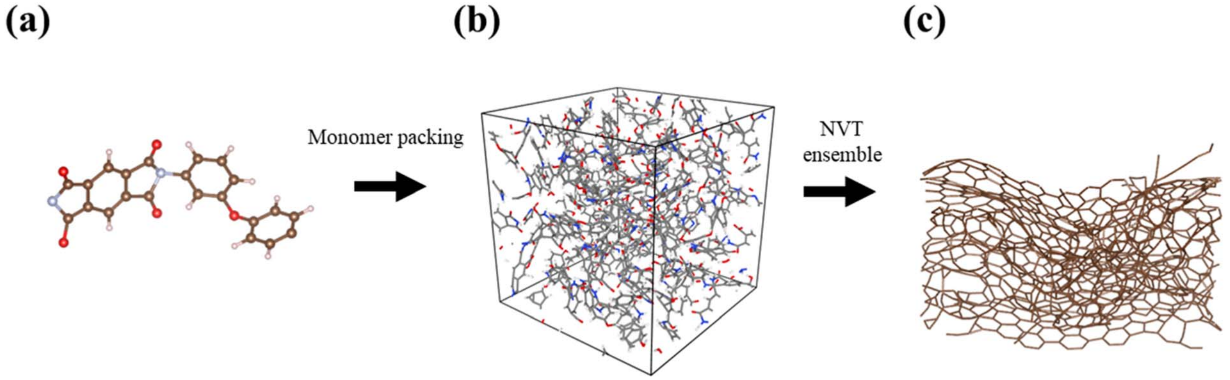

Fig. 2 Progress of a molecular dynamics simulation. (a) Kapton monomer modelling, (b) simulation cell, and (c) result of the ReaxFF simulation.

for 1 ns. The cooling process was performed at 300 K for 0.5 ns to create realistic conditions.

Results and discussion

Fig. 3 shows the FE-SEM measurements of the area corresponding to different laser fluences, each varying with the laser focus. The images intuitively illustrate the relationship between fluence and particle size. The surface of the PI exhibits porous pores of size 5–10 μm, which are caused by the release of gases, such as H_2, CO, H_2O, and NH_3, under instantaneous high temperature and pressure conditions.[40–42] These mechanisms are explained later using the results of the MD simulations.

Fig. 3(b) shows the PI surface at a fluence of 5.45 J cm^{-2}. At this laser fluence, nanocarbon particles were synthesised with diameters ranging from 12.1 to 254.5 nm and a mean ECD of

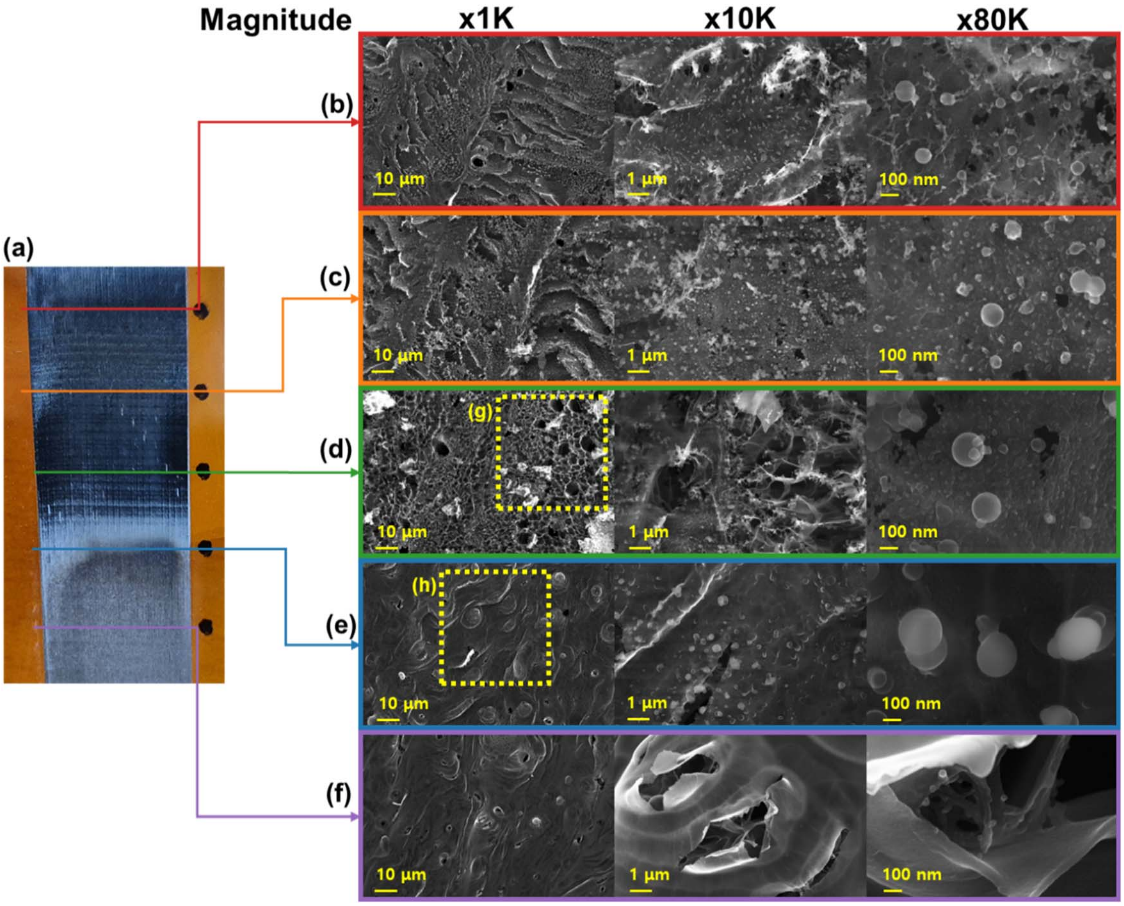

Fig. 3 (a) Photograph of the laser-processed PI film. FE-SEM images of the fabricated film at laser fluence of (b) 5.45 J cm^{-2}, (c) 2.35 J cm^{-2}, (d) 1.30 J cm^{-2}, (e) 0.83 J cm^{-2}, and (f) 0.57 J cm^{-2}. (g) Represents opened pore structure, and (h) indicates hill-like structure.

62.7 ± 40.0 nm, indicating significant particle growth and a wide size distribution. Fig. 3(c) presents the results of processing at a fluence of 2.35 J cm^{-2}, where the porosity of the surface layer increased compared to the previous fluence level, and the particle size slightly decreased, ranging from 12.1 to 292.6 nm with a mean ECD of 59.3 nm. Therefore, an increase in the fluence affects the formation and aggregation of carbon particles. During this process, the particles were subjected to an instantaneous high temperature through a laser pulse, and the pyrolysed carbons on the PI surface aggregated to form amorphous carbon spheres with minimal surface energy.

Fig. 3(d) depicts the results at a higher fluence of 1.30 J cm^{-2}, where an opened pore structure (Fig. 3(g)) was formed that had the highest porosity of all results.[29] The diameter of the carbon nanospheres (CNSs) ranged from 12.8 to 277.1 nm, with a mean ECD of 51.1 nm, representing the formation of larger aggregates under these conditions. This was attributed to the gaseous decomposition of the constituent atoms on the molten PI surface, which promoted the formation of a porous structure.

Fig. 3(e) corresponds to 0.83 J cm^{-2}, where the surface morphology transitioned to a hill-like structure with reduced porosity (Fig. 3(h)); the particles ranged from 12.3 to 454.8 nm, and the mean ECD increased to 64.2 nm with the highest standard deviation observed (67.3 nm), suggesting highly heterogeneous particle formation.

Fig. 3(f) presents the results at the lowest fluence of 0.57 J cm^{-2}, where almost no CNSs were observed and the maximum particle size decreased, with diameters up to 46.1 nm and a mean ECD of 9.2 nm. This suggests the existence of an optimal fluence for carbon particle formation. The diameters of the particles formed at each location varied based on the fluence conditions. These results showed that the size and shape of the CNSs could be effectively controlled by precisely adjusting the parameters of the pulsed laser.

Fig. 4 shows the size distribution of the CNSs under different laser fluences using histograms with red KDE curves. Right-skewed distributions indicate the presence of a small number of large particles. Fig. S1† is a schematic representation of the effect of nanostructure formation on fluence. At the highest fluence (a) of 5.45 J cm^{-2}, both the mean diameter (62.7 nm) and standard deviation (SD) are relatively large, suggesting a broad size distribution. In contrast, at the lowest fluence (e) of 0.57 J cm^{-2}, there is a significant reduction in the mean ECD (9.2 nm) with a narrow distribution range, implying that particle formation was significantly suppressed to produce only small particles. As the fluence increased, both the mean particle size and size distribution range tended to increase, demonstrating a positive correlation between laser energy and particle size heterogeneity. At a high fluence, more energy is concentrated in a shorter time, causing sharp localised increases in the temperature in the heated area and cooling. This results in a non-uniform temperature distribution during pulsed laser processing, which is the main cause of the increasing deviations in the size distribution of the particles produced.[43] Especially for materials with low thermal conductivity, the heat spreads less quickly, resulting in the formation of localised hot spots, which can be interpreted as asymmetrical thermal deformation.

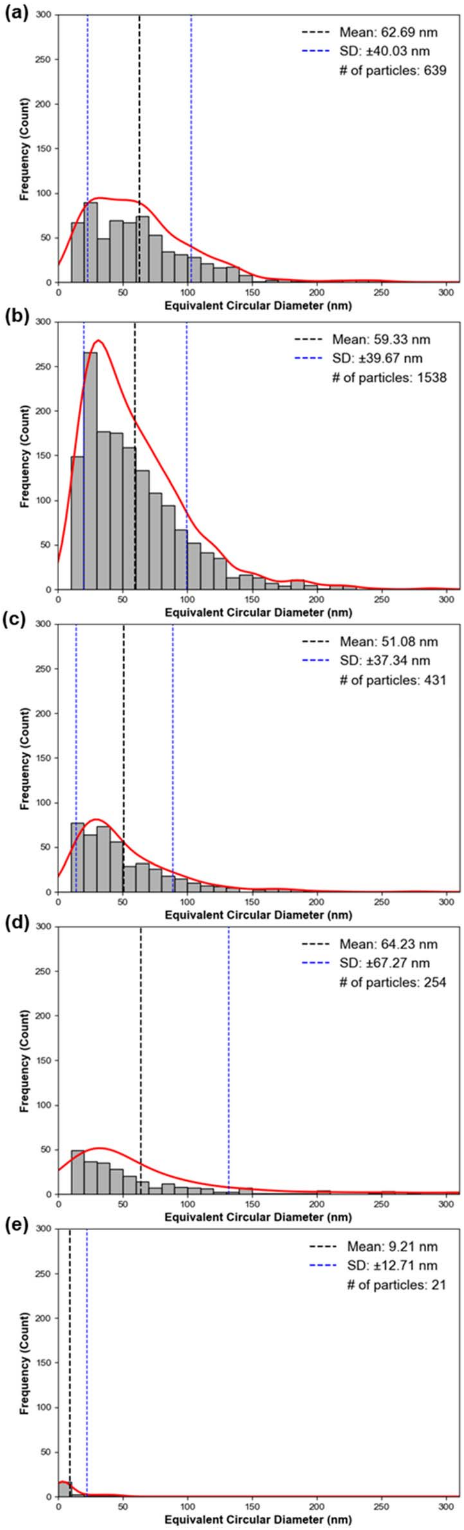

Fig. 4 ECD distribution of particles formed at different laser fluences of (a) 5.45 J cm^{-2}, (b) 2.35 J cm^{-2}, (c) 1.30 J cm^{-2}, (d) 0.83 J cm^{-2}, and (e) 0.57 J cm^{-2}. Each plot includes a histogram of the particle counts, the scaled KDE curve (red), and the mean ECD (black dashed line) with the standard deviation (blue dashed lines).

Notably, at 0.83 J cm^{-2}, the mean size remain moderate; however, the standard deviation is the highest among all the conditions, which may suggest unstable thermal or aggregation dynamics during carbon material formation.[41] This is because at low fluences, there is insufficient carbonisation and vaporisation, leading to cross-linking. Conversely, at large fluences, rapid vaporisation hinders formation of stable structures.[44] This will be discussed in detail in the section on the quantitative analysis of hybridisation structures. Maximova *et al.* reported a non-monotonic phenomenon in laser-assisted nanoparticle synthesis, in which the particle size increases with increasing energy and then decreases beyond a certain energy.[45] In this study, the energy-dependent differences in the binding energy of carbon resulted in a non-monotonic pattern in the number and size of the generated particles. These findings confirm that both particle shape and particle growth behaviour are highly dependent on the laser fluence. Therefore, the precise control of the fluence can serve as an effective strategy to promote the uniformity of the nanospheres produced.

To analyse the effect of temperature on carbon structure formation, the MD images created at different temperatures were analysed. Fig. 5 shows the conformational evolution over time at 3800, 4200, 4600, and 5000 K. The high temperature was maintained for 1 ns, followed by cooling to 300 K for 0.5 ns. As the temperature increased, PI dissolved through thermal decomposition and subsequent intercarbon recombination to form sp^2 or sp^3 hybridized structures. Here, sp^3 affects the three-dimensional stereochemistry of the carbon structure, resulting in a disordered three-dimensional morphology that contrasts with the two-dimensional structure of graphene. At relatively low temperatures, in the 3800 K range, π-bonds are dominant, and a two-dimensional planar structure of 5-, 6-, and 7-membered carbon rings is formed. As the temperature increased, the proportion of sp^3 bonds increased, in which a single carbon bonded with four other carbons to form a three-dimensional bond, and each of these structures formed a carbon sphere. This result is consistent with the previous atomic simulations using the second-generation REBO potential, which showed that small carbon clusters (C_n, $11 \leq n \leq 55$) evolve from planar sp^2-bonded ring structures at low sizes ($n \leq 18$) to non-planar, three-dimensional morphologies containing sp^3 hybridised atoms at larger sizes ($n \geq 19$).[46] Furthermore, it also supports the finding that the combination of hexagonal carbon rings with pentagonal and heptagonal carbon rings forms a curved structure, resulting in a three-dimensional surface.[47]

Vashisth *et al.* found through MD simulations that the optimum temperature for LIG is 3000 K. Simulations were performed at higher temperatures (3800, 4200, 4600, and 5000 K).[42] Fig. 6 presents the evolution of the structure at 3800 K. The graphene layers exhibited a *d*-spacing distance of 3.48 Å or 3.55 Å, depending on the position. This is slightly higher than the *d*-

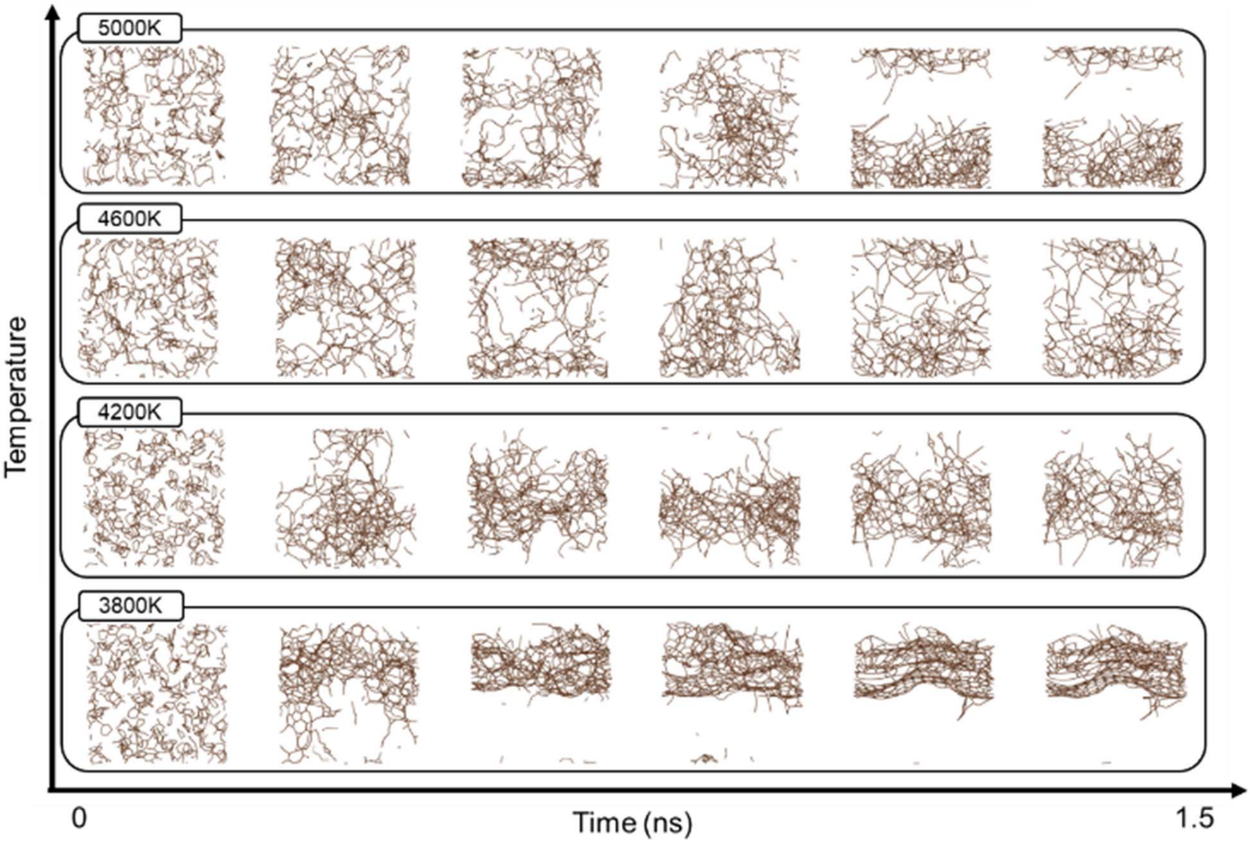

Fig. 5 Evolution of PI over time as a function of temperature (3800, 4200, 4600, and 5000 K).

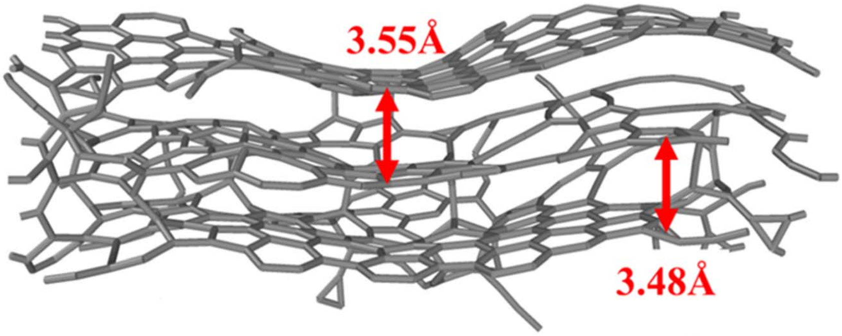

Fig. 6 *d*-Spacing distance between three graphene planes formed at a temperature of 3800 K.

spacing distance of 3.4 Å reported by Huang *et al.*[48] This difference suggests an increase in interlayer distance, probably owing to thermal expansion or structural instability induced by high temperature, indicating that the graphene structure begins to destabilize around 3800 K. This result was further supported by the radial distribution function (RDF) analysis shown in Fig. S2.† The RDF shows short-range peaks at distances shorter than the interlayer spacing of graphite (∼3.4 Å) as the temperature increases, suggesting that interlayer collapse or structural buckling may occur owing to thermal instability.

Raman spectroscopy was used to evaluate structural changes in the laser-processed PI. The Raman spectrum of a material contains optical information on each molecule. In the Raman spectrum shown in Fig. 7, two dominant peaks were observed, corresponding to the D band (1343 cm^{-1}) and G band (1581 cm^{-1}), respectively. The D band is related to the defects of sp^2 carbon in the amorphous carbon structure, and is affected by inelastic phonon scattering in polycrystalline graphite.[49] The G band corresponds to the bond-stretching vibrations of the carbon network. A 2D peak is present at 2692 cm^{-1}, but considerably weak, demonstrating that no crystallised graphene was formed.[50] The intensity ratio I_D/I_G of the D and G bands was measured to be 1.02, indicating that the carbon structure produced after laser processing is amorphous carbon with a relatively retained sp^2 structure. According to the amorphization trajectory, the observed G-band position and I_D/I_G ratio place the laser-processed PI near the boundary between nanocrystalline graphite and amorphous carbon.[51,52] Therefore, while the sp^2 bonding network remains partially preserved during laser processing, the long-range crystallinity is disrupted.

Simulations were conducted at four different temperatures, from 3800 to 5000 K, to analyse the changes in the carbon

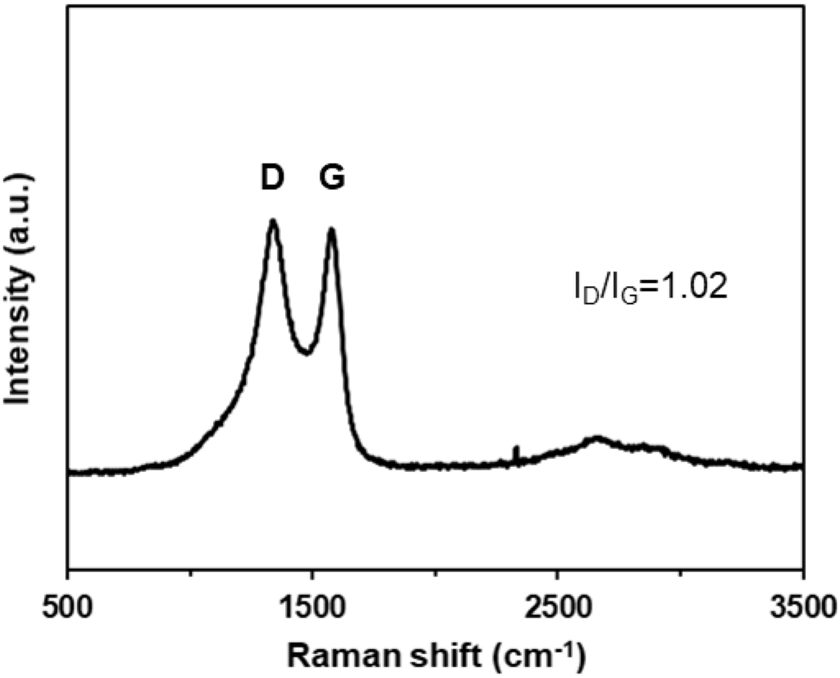

Fig. 7 Raman spectrum of the LIG-irradiated 450 nm pulsed laser.

structure with temperature. After pyrolysis, the carbon atoms were observed to aggregate and form various hybridisation structures (sp^2, sp^3). Fig. 8 quantitatively highlights the number of these structures.

Fig. 8(a) shows the recorded number of sp^2 structures as a function of time. This number decreases as the temperature increases, suggesting that graphene structures do not readily form at high temperatures. Fig. 8(b) represents the number of sp^3 structures, which increased with temperature, peaking at 4200 K before subsequently decreasing.

The ratio of sp^2 and sp^3 structures change continuously over time; thus, the sp^3/sp^2 ratio was analysed as a key metric. The results reveal that the ratio peaked at 1 : 10 at 4200 K, as shown in Fig. 8(c). Fig. 8(d) shows the average for each temperature of sp^3/sp^2 formation over the time of the simulation, attaining the highest values at 4200 K. This ratio suggests an amorphous carbon structure rather than perfect crystallinity, demonstrating that there are limited sp^3 bonds and carbon structure is disordered.

Additionally, in this simulation, a distinct increase in the proportion of sp^3 carbon bonds at 4200 K was observed; the number of sp^3 and sp^2 structures tended to decrease as the temperature exceeded 4600 K. This can be interpreted as a temperature-driven structural phase transition and breakdown of bonds owing to energetic instability. The thermal energies of the carbon atoms surpass the π-bond energy (272 kcal mol^{-1})[53] and σ-bond energy (345 kJ mol^{-1}), leading to bond dissociation.[54] At high temperatures, structural bonding undergoes ring breakdown, temporarily favouring the formation of sp^3-based amorphous carbon structures. In the ultrahigh temperature region above 3700 K, sp^2 carbon ring structures composed of π-bonds collapse, while sp^3 structures composed of only σ-bonds remain relatively stable. This is a critical point explaining the increase in the sp^3 bond ratio at 4200 K from an energy perspective. As the energy increases beyond this point, the ratio decreases due to the difficulty in maintaining stable bonds, as shown in Fig. 4(d). Moreover, thermal vibrations can distort the bond angles and destabilise the structure. Consequently, we can confirm the existence of an optimal temperature range conducive to sp^3 structure formation, providing significant insight into the development of three-dimensional carbon structures.

During the simulation, the occurrence of H_2, NH_3, H_2O, and CO was monitored because these gases are produced as the PI is thermally decomposed and reconstituted. These gases influenced the formation of pores in the film. Fig. 9 highlights the development of each gas molecule over time. Fig. 9(a and b) present the evolution of H_2 and NH_3, respectively, revealing weak growth over time at temperatures up to 5000 K. This indicates that the carbon structure was rearranged during the

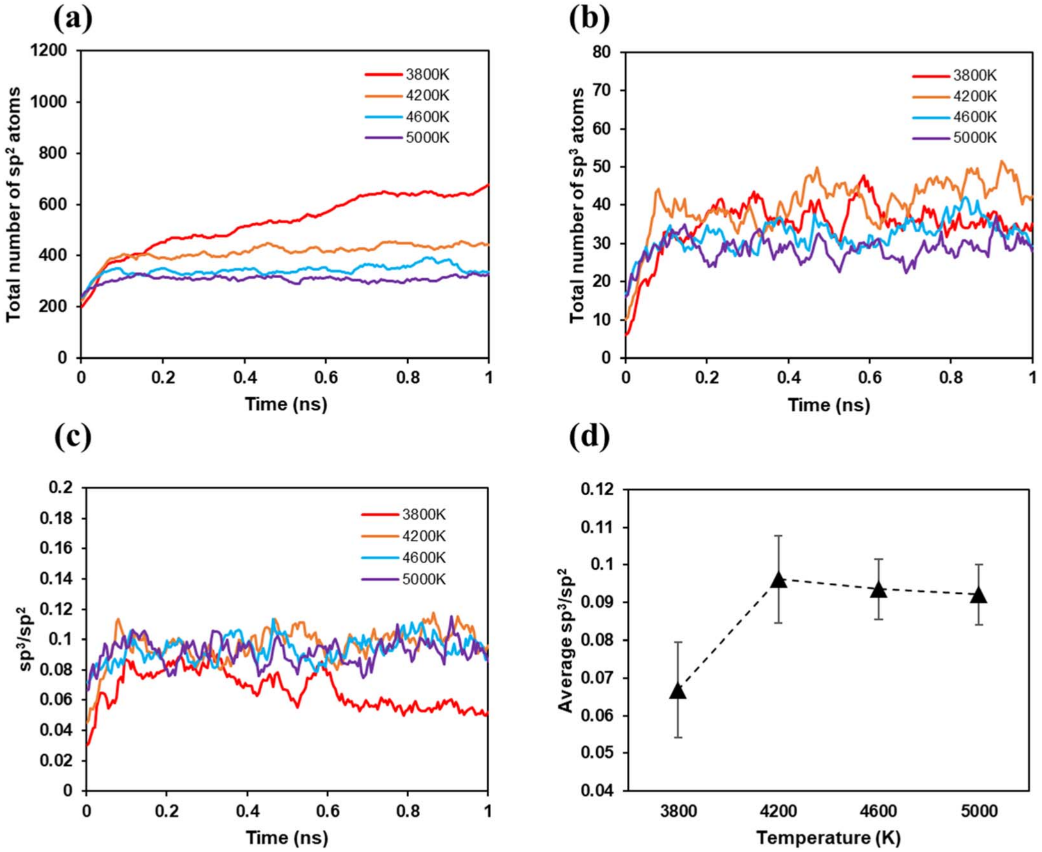

Fig. 8 Evolution of the values for (a) total number of sp^2 and (b) sp^3 atoms, (c) sp^3/sp^2 over time as a function of temperature (3800, 4200, 4600, and 5000 K), and (d) average ratio.

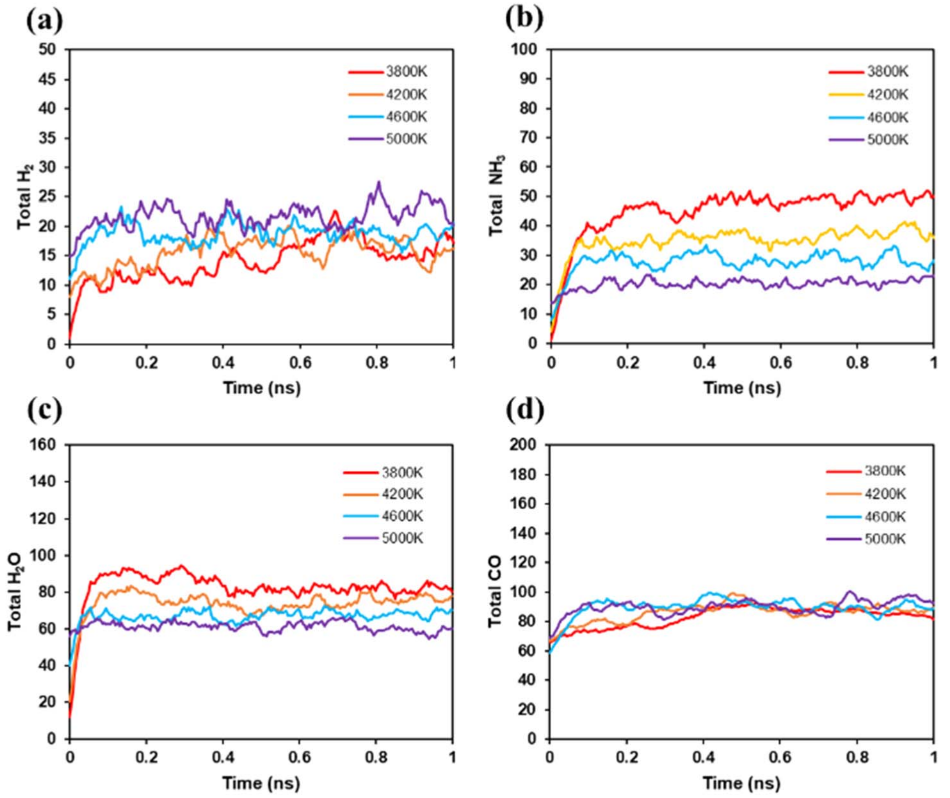

Fig. 9 Number of (a) H_2O, (b) NH_3, (c) H_2O, and (d) CO molecules released over time as a function of temperature (3800, 4200, 4600, and 5000 K).

pyrolysis process, releasing residual hydrogen as H_2. In addition, NH_3 release may increase as the imide structure of the polyimide decomposes at higher temperatures. Fig. 9(c) shows the opposite effect for dehydration, where H_2O decreases over time. Therefore, at extremely high temperatures, H_2O may oxidise other gases, thereby contributing to the formation of CO or CO_2. In addition, as shown in Fig. 9(d), CO remained constant over time at most temperatures. The laser fluence caused differences in the proportion of gases emitted, indicating that this was a controllable factor.

Fig. S3† quantitatively illustrates the total number of H_2, NH_3, H_2O, and CO molecules generated under each temperature condition. At all temperatures, the number of gas molecules increases up to 0.1 ns and then remains constant after 0.2 ns. This trend is consistent with the sp^3 content and sp^3/sp^2 ratio shown in Fig. 8(b) and (c), indicating the stabilisation of the bonding structure within the system.

As the laser fluence increased, the amount of gas produced decreased slightly, which affected the formation of a porous pattern in the laser-processed regions. This phenomenon was consistent with the findings of Dong *et al.*, who performed MD simulations of polyimide. They reported that even at elevated annealing temperatures, the final yield of small molecules did not necessarily increase. However, at high temperatures, a sharp reduction in the number of 6-membered rings occurs, causing the simultaneous structural collapse and reorganisation of the carbon network, resulting in recrystallisation into graphitic structures.[55]

These results suggest that a higher fluence accelerates the removal of noncarbon elements and promotes the rearrangement of carbon hybridisation structures, which may suppress gas formation while enhancing the crystallinity of the carbon nanostructures. X. Lu *et al.* reported that under high-temperature and high-energy conditions, secondary reactions facilitate the dissociation of heteroatomic bonds, such as C–N and C–O, which promote both the elimination of non-carbon species and reconstruction of the carbon backbone.[56]

Therefore, we propose that the effect of fluence is as follows: gas evolution induces the elimination of heteroatoms from the carbon network and facilitates the formation of carbon hybridisation structures; however, under excessively high-energy conditions, bond energy mismatches can cause network collapse.

Consequently, optimising the fluence conditions can help balance carbon nanostructure formation and pore pattern development. This interpretation is consistent with the findings of Maximova *et al.*, who reported that morphological and porosity changes in nanostructures depend on the applied laser energy.[45]

Conclusions

In this study, we proposed a novel laser-based process for synthesising CNSs from PI films using a nanosecond-pulsed laser with a wavelength of 450 nm. By adjusting the laser fluence, we controlled the size of the CNSs produced, demonstrating a correlation between laser energy and particle size. In particular, quantitative indicators, such as the number of particles, average size, and standard deviation of the size distribution, were closely analysed for variable effects through specific analyses. The optimized fluence of 2.35 J cm^{-2} resulted in the highest number of particles, representing a 140% and 257% increase compared to 5.45 J cm^{-2} and 1.30 J cm^{-2}, respectively.

MD simulations were performed to elucidate the mechanism of CNS formation under various thermal conditions, revealing that the sp^3 hybridisation ratio peaks at 12% at approximately 4200 K, which is the optimal temperature for forming a stable three-dimensional structure. This result agrees with the experimental observations of the nanospheres, where the sp^3 hybridisation ratio peaked because of the increased structural stability provided by the sp^3 bonding environments under these thermal conditions. Notably, the simulations traced the atomic-level transition behaviour and bonding formation mechanism, which are difficult to observe experimentally, providing important insights into the controllability of the structure under laser conditions.

However, because the simulation time in this study was limited to 1 ns, which may differ from the actual processing conditions, future studies should extend the simulation timescale and refine the laser processing conditions to achieve more precise control over the CNS morphology. Further research is required in several areas: (1) the implementation of nanosphere formation within MD to verify the fidelity, (2) detailed characterisation of the internal structures and compositions of the CNS, and (3) the development of a scalable, non-toxic synthesis for mass production.

Data availability

The datasets used and analysed during the current study are available from the corresponding author on reasonable request.

Author contributions

The contributions of the authors to this study are as follows: Cheol Hwan Kim, Chae Yoon Shin, and Jun Uk Lee contributed equally to this work. Cheol Hwan Kim conducted the MD simulations, compiled and analysed the data, performed Raman spectroscopy measurements, and drafted the manuscript. Chae Yoon Shin performed the FE-SEM measurements and laser-processing experiments, created the figures, analysed the data, and drafted the manuscript. Jun Uk Lee presented a processing method for the formation of nanoparticles. Sung-Yeob Jeong reviewed the MD simulation methods (co-corresponding author). Bo Sung Shin provided the experimental guidance and supervised the manuscript (co-corresponding author).

Conflicts of interest

There are no conflicts to declare.

Acknowledgements

This work was supported by the Korea Institute for Advancement of Technology Fund grant funded by the Republic of Korea Ministry of Trade, Industry and Energy (Project Number: RS-2024-00411221). This work was supported by 2025 Specialization Project of Pusan National University. This research was also supported by a Korea Basic Science Institute (National Research Facilities and Equipment Center) grant funded by the Republic of Korea Ministry of Education (Grant Number: 2021R1A6C101A449).

References

1 A. Lu, G. Hao, Q. Sun, X. Zhang and W. Li, *Chem. Synth. Appl. Graphene Carbon Mater.*, 2017, pp. 115–157.
2 A. O. Egbedina, O. P. Bolade, U. Ewuzie and E. C. Lima, *J. Environ. Chem. Eng.*, 2022, **10**(2), 107260.
3 C. Kim, K. Kim and J. H. Moon, *Sci. Rep.*, 2017, **7**(1), 14400.
4 S. Singh, T. S. S. K. Naik, B. Uppara, P. Narasimhappa, R. Varshney, V. Chauhan, N. Shehata, C. Thamaraiselvan, S. Subramanian, J. Singh, N. A. Khan, S. Zahmatkesh, L. Singh and P. C. Ramamurthy, *Chemosphere*, 2023, **328**, 138533.
5 Y. Fang, D. Gu, Y. Zou, Z. Wu, F. Li, R. Che, Y. Deng, B. Tu and D. Zhao, *Angew. Chem., Int. Ed.*, 2010, **49**, 7987–7991.
6 Q. Ge, H. Yu, L. Zhang, S. Ni, W. Wu, H. Yang, J. Liu and K. Huang, *Microporous Mesoporous Mater.*, 2022, **336**, 111865.
7 Y. Yao, J. Xu, Y. Huang and T. Zhang, Synthesis and applications of carbon nanospheres: A review, *Particuology*, 2024, **87**, 325–338.
8 D. Wang, A. Fu, H. Li, Y. Wang, P. Guo, J. Liu and X. S. Zhao, *J. Power Sources*, 2015, **285**, 469–477.
9 B. Fang, J. H. Kim, M.-S. Kim and J.-S. Yu, *Acc. Chem. Res.*, 2013, **46**, 1397–1406.
10 J.-G. Wang, H. Liu, H. Sun, W. Hua, H. Wang, X. Liu and B. Wei, *Carbon*, 2018, **127**, 85–92.
11 L. Liu, X. Sun, Y. Dong, D. Wang, Z. Wang, Z. Jiang, A. Li, X. Chen and H. Song, *J. Power Sources*, 2021, **506**, 230170.
12 D. Jung, G. Duman, M. Zimmermann, A. Kruse and J. Yanik, *Biomass Convers. Biorefin.*, 2023, **13**(7), 6281–6297.
13 J. Zhu, J. Wang, G. Li, L. Huang, M. Cao and Y. Wu, *J. Mater. Chem. A*, 2020, **8**, 25746–25755.
14 W. Stöber, A. Fink and E. Bohn, *J. Colloid Interface Sci.*, 1968, **26**, 62–69.
15 X. Li, Z. Liu, C. Cai, Q. Yu, W. Jin, M. Xu, C. Yu, S. Li, L. Zhou and L. Mai, *ChemSusChem*, 2021, **14**, 1756–1762.
16 C. Liu, J. Wang, J. Li, X. Hu, P. Lin, J. Shen, X. Sun, W. Han and L. Wang, *J. Mater. Chem. A*, 2016, **4**, 11916–11923.
17 M. Mezhericher, J. K. Nunes, J. J. Guzowski and H. A. Stone, *Chem. Eng. J.*, 2018, **346**, 606–620.
18 X. Li, J. Zhou, J. wang, W. Qiao, L. Ling and D. Long, *RSC Adv.*, 2014, **4**, 62662–62665.
19 C. Wang, Y. Wang, J. Graser, R. Zhao, F. Gao and M. J. O'Connell, *ACS Nano*, 2013, **7**, 11156–11165.
20 G. G. Karthikeyan, G. Boopathi and A. Pandurangan, *ACS Omega*, 2018, **3**, 16658–16671.

21 Z. G. Liu, X. X. He, J. H. Zhao, C. M. Xu, Y. Qiao, L. Li and S.-L. Chou, *Chem. Commun.*, 2023, **59**, 4257–4273.

22 F. Xu, Z. Tang, S. Huang, L. Chen, Y. Liang, W. Mai and D. Wu, *Nat. Commun.*, 2015, **6**(1), 7221.

23 Z. Wu, W. Li, P. A. Webley and D. Zhao, *Adv. Mater.*, 2012, **24**, 485–491.

24 H. Tian, J. Liang and J. Liu, *Adv. Mater.*, 2019, **31**, 1903886.

25 G. K. Yogesh, S. Shukla, D. Sastikumar and P. Koinkar, *Appl. Phys. A: Mater. Sci. Process.*, 2021, **127**, 1–40.

26 L. Zhao, Z. Liu, D. Chen, F. Liu, Z. Yang, X. Li and W. Zhou, *Nano-Micro Lett.*, 2021, **13**, 1–48.

27 K. Bagga, R. McCann, M. Wang, A. Stalcup, M. Vázquez and D. Brabazon, *J. Colloid Interface Sci.*, 2015, **447**, 263–268.

28 S. L. Shumlas, K. M. Tibbetts, J. H. Odhner, D. A. Romanov, R. J. Levis and D. R. Strongin, *Mater. Chem. Phys.*, 2015, **156**, 47–53.

29 S. Hong, J. Kim, S. Jung, J. Lee and B. S. Shin, *ACS Mater. Lett.*, 2023, **5**, 1261–1270.

30 V. G. Pol, J. Wen, K. C. Lau, S. Callear, D. T. Bowron, C.-K. Lin, S. A. Deshmukh, S. Sankaranarayanan, L. A. Curtiss, W. I. F. David, D. J. Miller and M. M. Thackeray, *Carbon*, 2014, **68**, 104–111.

31 Y. Zhao, Y. Zhao, F. Wu, Y. Zhao, Y. Wang, C. Sui, X. He, C. Wang, H. Tan and C. Wang, *Carbon*, 2021, **173**, 600–608.

32 A. C. T. Van Duin, S. Dasgupta, F. Lorant and W. A. Goddard, *J. Phys. Chem. A*, 2001, **105**, 9396–9409.

33 A. Ghavipanjeh and S. Sadeghzadeh, *Sci. Rep.*, 2024, **14**, 4475.

34 T. Kato, Y. Yamada, Y. Nishikawa, H. Ishikawa and S. Sato, *Carbon*, 2021, **178**, 58–80.

35 C. D. Wu, N. Y. Yeh and P. C. Cheng, *J. Mol. Model.*, 2024, **30**(2), 28.

36 Y. Bian, W. Zhang, T. Wu and D. Wang, *Phys. Chem. Chem. Phys.*, 2025, **27**, 12584–12592.

37 K. Li, H. Zhang, G. Li, J. Zhang, M. Bouhadja, Z. Liu and M. Barati, *J. Chem. Theory Comput.*, 2018, **14**(5), 2322–2331.

38 E. P. Cox, *J. Paleontol.*, 1927, **1**, 179–183.

39 D. W. Scott, *Biometrika*, 1979, **66**, 605–610.

40 L. Wang, Z. Wang, A. N. Bakhtiyari and H. Zheng, *Micromachines*, 2020, **11**, 1094.

41 X. Chen, C. Wang, M. Song, J. Ma, T. Ye and W. Xia, *Carbon*, 2019, **155**, 521–530.

42 A. Vashisth, M. Kowalik, J. C. Gerringer, C. Ashraf, A. C. T. van Duin and M. J. Green, *ACS Appl. Nano Mater.*, 2020, **3**, 1881–1890.

43 J. Theerthagiri, *et al.*, *Light: Sci. Appl.*, 2022, **11**(1), 250.

44 S.-Y. Jeong, *et al.*, *ACS Appl. Mater. Interfaces*, 2024, **16**(26), 33943–33953.

45 K. Maximova, *et al.*, *Nanotechnology*, 2015, **26**, 065601.

46 A. N. Mohan and B. Manoj, *Int. J. Electrochem. Sci.*, 2012, **7**, 9537–9549.

47 Z. L. Wang and Z. C. Kang, *J. Phys. Chem.*, 1996, **100**, 17725–17731.

48 L. Huang, J. Su, Y. Song and R. Ye, *Nano-Micro Lett.*, 2020, **12**, 1–17.

49 F. Mahmood, H. Zhang, J. Lin and C. Wan, *ACS Omega*, 2020, **5**, 14611–14618.

50 M. S. Dresselhaus, A. Jorio, M. Hofmann, G. Dresselhaus and R. Saito, *Nano Lett.*, 2010, **10**, 751–758.

51 A. C. Ferrari, *Diamond Relat. Mater.*, 2002, **11**, 1053–1061.

52 J. Kang, O. L. Li and N. Saito, *Carbon*, 2013, **60**, 292–298.

53 S. R. Kass, *J. Org. Chem.*, 2024, **89**, 15158–15163.

54 S. Kumbar, S. Patil and C. Jarali, in *Comprehensive Analytical Chemistry*, Elsevier, 2020, vol. 91, pp. 49–72.

55 Y. Dong, S. C. Rismiller and J. Lin, *Carbon*, 2016, **104**, 47–55.

56 X. Lu, X. Wang, Q. Li, X. Huang, S. Han and G. Wang, *Polym. Degrad. Stab.*, 2015, **114**, 72–80.